Vol. 91 No. 3 pp. 1025–1040 ACTA GEOLOGICA SINICA (English Edition) June 2017

Genesis of the Ciemas Gold Deposit and Relationship with Epithermal Deposits in West Java, Indonesia: Constraints from Fluid Inclusions and Stable Isotopes

ZHENG Chaofei[1, 2], ZHANG Zhengwei[1, *], WU Chengquan[1, 2] and YAO Junhua [1, 2]

1 *State Key Laboratory of Ore Deposit Geochemistry, Institute of Geochemistry, Chinese Academy of Sciences, Guiyang 550081, China*

2 *University of Chinese Academy of Sciences, Beijing 100049, China*

Abstract: The Ciemas gold deposit is located in West Java of Indonesia, which is a Cenozoic magmatism belt resulting from the Indo-Australian plate subducting under the Eurasian plate. Two different volcanic rock belts and associated epithermal deposits are distributed in West Java: the younger late Miocene–Pliocene magmatic belt generated the Pliocene–Pleistocene epithermal deposits, while the older late Eocene–early Miocene magmatic belt generated the Miocene epithermal deposits. To constrain the physico-chemical conditions and the origin of the ore fluid in Ciemas, a detailed study of ore petrography, fluid inclusions, laser Raman spectroscopy, oxygen-hydrogen isotopes for quartz was conducted. The results show that hydrothermal pyrite and quartz are widespread, hydrothermal alteration is well developed, and that leaching structures such as vuggy rocks and extension structures such as comb quartz are common. Fluid inclusions in quartz are mainly liquid-rich two phase inclusions, with fluid compositions in the NaCl-H_2O fluid system, and contain no or little CO_2. Their homogenization temperatures cluster around 240°C–320°C, the salinities lie in the range of 14–17 wt.% NaCl equiv, and the calculated fluid densities are 0.65–1.00 g/cm^3. The values of $\delta^{18}O_{H2O\text{-}VSMOW}$ for quartz range from +5.5‰ to +7.7‰, the δD_{VSMOW} of fluid inclusions in quartz ranges from −70‰ to −115‰. All of these data indicate that mixing of magmatic fluid with meteoric water resulted in the formation of the Ciemas deposit. A comparison among gold deposits of West Java suggests that Miocene epithermal ore deposits in the southernmost part of West Java were more affected by magmatic fluids and exhibit a higher degree of sulfidation than those of Pliocene–Pleistocene.

Key words: fluid inclusions, oxygen and hydrogen isotopes, epithermal, subduction, Ciemas gold deposit, West Java, Indonesia

1 Introduction

West Java, which is on the southern edge of the Sunda Continent (Fig. 1a), contains two distinctive Cenozoic magmatic belts resulting from subduction of the Indo-Australian plate beneath the Eurasian plate. The younger is a late Miocene–Pliocene magmatic belt in the south of Bogor, and the older is a late Eocene-early Miocene magmatic belt on the south of Ratu (Fig. 1b) (Soeria-Atmadja et al., 1994; Clements and Hall, 2007). In the former belt, low sulfidation epithermal gold-silver deposits with a Pliocene–Pleistocene mineralization age have historically been mined and are known for their substantial resources, including Pongkor (over 100 tons of gold and 1000 tons of silver) (Milesi et al., 1999), Cirotan (the historical gold mine center in Java) (Milesi et al., 1994), and Cikidang (Rosana and Matsueda, 2002) (Fig. 1b). In the latter older magmatic belt, several gold deposits or prospects with Miocene mineralization ages have recently been explored and studied, including the Cijulang prospect (Tun et al., 2014a, 2014b), the Arinem deposit (Yuningsih et al., 2012; Yuningsih and Matsueda, 2014), the Cibaliung deposit (Harijoko et al., 2004; Harijoko et al., 2007), and the Ciemas deposit (Wu et al., 2014; Zheng Chaofei et al., 2014; Zhang et al., 2015) (Fig. 1b). The ore deposits in the older magmatic rock belt can be classified into low sulfidation (Cibaliung), high sulfidation (Cijulang), and low sulfidation overprinted by high

* Corresponding author. E-mail: zhangzhengwei@vip.gyig.ac.cn

sulfidation (Arinem), and their mineralization ages are concentrated in the late Miocene. Based on the results of exploration and previous studies, the Ciemas deposit exhibits the distinctive characteristics of the trinity pattern of Au deposit and is defined as an epithermal to porphyry type related to the Miocene arc magmatism (Zhang et al., 2015). The igneous host rocks of Ciemas are also the oldest among all the deposits of West Java, with an age of ~17 Ma (Wu et al., 2014).

To better understand the nature of the mineralization in Ciemas, it is important to conduct a study on the ore-forming fluids, and make a comparison with the other gold deposits in West Java. In this paper, the characteristics of the fluid inclusions, and oxygen and hydrogen isotopes, as well as the ore structures and textures of Ciemas are documented. And then, the ore genesis, as well as the ore fluid sources and the precipitation mechanisms are presented. Finally, the spatial and temporal variations among the epithermal deposits in West Java are demonstrated.

2 Geological Setting

2.1 Regional geology

West Java is located in the central-west region of the Sunda-Banda continental arc (Fig. 1a), which is a typical convergent plate margin (Marcoux and Milési, 1994; Clements and Hall, 2007). The northward subduction of the Indio-Australia plate under the Eurasian plate began in the Late Cretaceous (Rosana and Matsueda, 2002; Wang Chengshu, 2002), and created an active continental margin magmatic belt (Fig. 1b).

Most of the exposed rocks are Tertiary volcanic breccia, tuff, andesite, as well as Quaternary residual deposits and alluvial deposits (Sukamto, 1975; Milesi et al., 1999; Jonathan, 2007). The exposed strata in the Ciemas mineralization zone include the Jampang Formation, the Cikarang Member and the Ciseureuh Member (Fig. 2a). The most widespread is the Tertiary Jampang Formation. The lower part of this formation consists of globigerina marl, sandstone, and calcareous brecciated tuff of andesitic and dacitic composition intercalated with thick limestone beds containing large foraminifera. The upper part consists of volcanic breccia tuff (locally containing nodules) and limestone lenses, with many andesitic to dacitic sills, dikes and quartz veins. The Cikarang Member consists of volcanic tuff, with interbedded pumice tuff, pumice sandstone, calcareous sandstone, andesitic, dacitic, and brecciated tuff. The Ciseureuh Member consists of andesite and basaltic lava flows, and partly brecciated pillow basalts (Sukamto, 1975; Jonathan, 2007).

The structures are mainly NW- and NE-trending faults

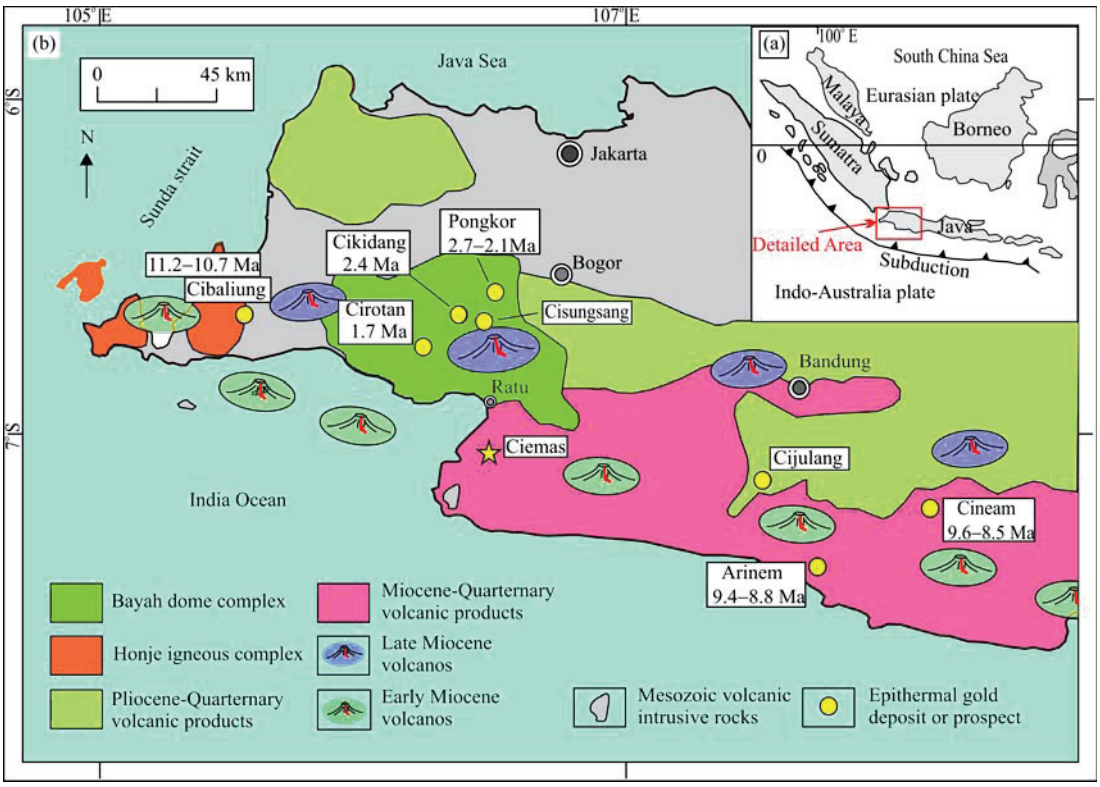

Fig. 1. Sketch geological map of West Java, Indonesia.
(a), Tectonic location map; (b), Regional geology and gold deposits distribution in West Java (modified after Marcoux and Milési, 1994; Tun et al., 2014a; Yuningsih et al., 2014; Zhang et al., 2015).

and folds (Fig. 2a). Reverse faults were developed in the Ciemas area. The main fold is the Ciemas syncline, with an NE-trending axis (Sukamto, 1975).

Late Cretaceous igneous complexes are exposed to the south of Ciemas, which were accreted at the south periphery of West Java (Wakita, 2000). While the most igneous rocks are widespread Cenozoic magmatic rocks, which are composed of andesitic volcaniclastic rocks and a small amount of andesitic to basaltic lavas. Dacite has been found within the Ciemas region. A small amount of Miocene (hornblende) quartz diorite porphyry (Fig. 3c) and fine-grained andesite dikes are present as intrusions into the older rocks in Ciemas (Fig. 2a–b).

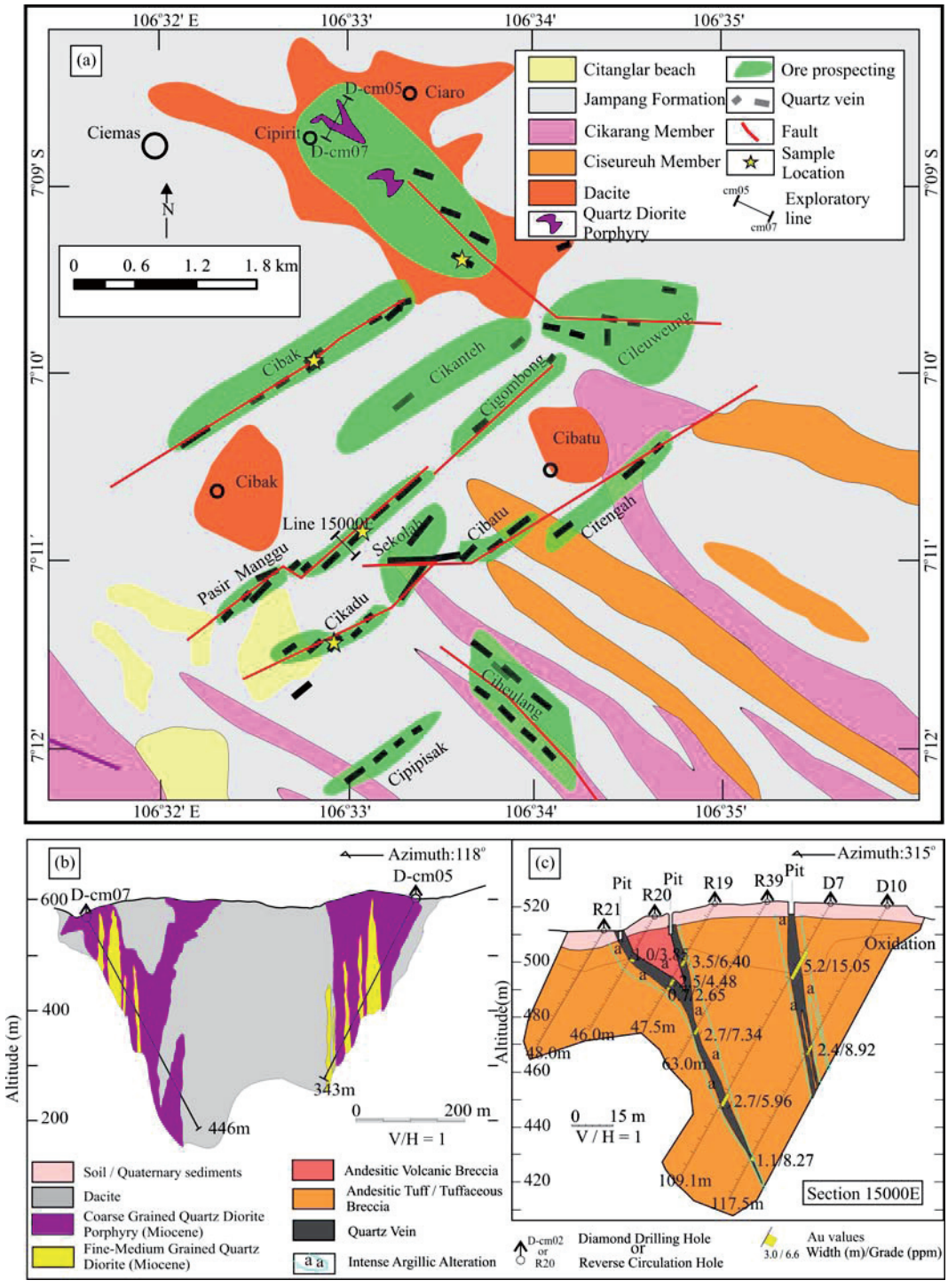

Fig. 2. (a), Simplified geological map of the Ciemas gold deposit; (b), Simplified geological section between drill holes D-cm05 and D-cm07 in Cipirit; (c), Geological section of the 15000E prospecting grid line in Pasir Manggu (modified after Jonathan, 2007; Gao et al., 2013; Zhang et al., 2015).

2.2 The Ciemas gold deposit

The Ciemas gold deposit contains eight major ore blocks, namely the Pasir Manggu, Cikadu, Sekolah, Cibatu, Cigombong, Cileuweung, Cibak, and Cipirit ore blocks. Through drilling investigations, the orebodies were found to occur mainly within the dacite and fracture zones (Jonathan, 2007). The orebodies are shaped as veins and layered veins, and are mostly NW-trending with some SE-trending, dipping 70–80° to the east. The major orebodies are generally several hundreds of meters long, with thicknesses of up to a few meters (Fig. 2c). The Au grade ranges from <2 g/t to >15 g/t (Fig. 2c), with 10–60 g/t Ag (with a maximum Ag grade of 512 g/t) (Gao et al., 2013).

The wall rock alteration types include potassic alteration, argillic alteration, pyritization, chloritization, silicification, carbonatization and epidotization. The propylitization (including chloritization, carbonatization and epidotization) mainly occurs in the periphery. The thickness of the alteration zones reach as much as 5 meters at the top of the orebody but become narrower at the footwall (Fig. 2c). The clay minerals consist of smectite, illite and kaolinite. In the Cipirit ore block, some siliceous clayization zones developed in the dacite and formed quartz stockwork.

3 Ore Structures and Textures

The ore types can be divided into quartz-sulfide vein ores (equivalent to the high-sulfur type) (Fig. 3a), structurally controlled alteration ores (Fig. 3b), and porphyry-hosted ores (Fig. 3c). Quartz-sulfide vein ores occur in the Pasir Manggu, Cibak, Cigombong, and Cileuweung ore blocks. Structurally controlled alteration ores are present in the Cikadu, Sekolah, and Cibatu ore blocks. Porphyry-hosted ores occur in the Cipirit ore block. The drilling results indicate that the quartz diorite porphyrite contains pyrite and chalcopyrite mineralization but with a low Au content (<0.1 ppm). However, in zones displaying silicification, pyritization, and propylitization, the Au content is generally over 1 ppm. Some of the mineralization occurs in the quartz diorite porphyry. In the porphyry bodies and the contact zone, porphyry copper and gold mineralization are developed. In the porphyry contacts and other volcanic rocks, quartz vein-type gold orebodies are found. Mineralization in rocks with structurally controlled alteration occurs in fault zones located far away from the porphyry. These different types of deposits, displaying the "trinity" in space, are genetically related (Zhang et al., 2015).

Metallic minerals mainly include pyrite, arsenopyrite, limonite (Fig. 3h, 3j; Fig. 4c), chalcopyrite, galena, sphalerite, bornite, marcasite, chalcocite, and rutile (Fig. 4f). The gangue minerals mainly consist of quartz, plagioclase, chlorite, sericite, biotite, smectite, illite, calcite, dolomite, and ferrodolomite. Pyrite is the most common metallic mineral and always contains arsenic. Quartz is the most common gangue mineral, with massive, vuggy, comb, crustiform and colloform structures, and is accompanied by partial chalcedonization. The most common mineral assemblage in the ores is the pyrite–gold–quartz association. Au exists independently in the form of native gold within quartz, arsenopyrite or in arsenic pyrite, or exists as invisible gold in arsenopyrite or arsenic pyrite. The Ag content exceeds 100 g/t in some ores such as in Pasir Manggu and Cileuweung. In addition, several scattered lead-zinc mineralized veins occur in the Cibatu and Cipirit blocks.

The ore structures include disseminated (Fig. 3d), stockwork (Fig. 3e), brecciated (Fig. 3f), massive (Fig. 3g) and vesicular/vuggy structures (Fig. 3h), in addition to quartz comb structures (Fig. 3i) and drusy/miarolitic structures (Fig. 3i). The structure of sulfides disseminating in the vuggy siliceous rocks is very typical and widely developed. Stockwork structure can be observed in the altered ores. The brecciated structure is characterized by late metal sulfides and quartz cementing volcanic tuff breccia. The massive ore structure occurs in the fractured zones, which may locally be nearly entirely filled with pyrite, and in places where the pyrite became very loose due to extensive water immersion in the near surface environment. The vesicular structure formed when dacite or quartz underwent leaching by acidic fluids and became porous. The pores are locally filled with sulfides which could be Au-bearing. The comb structure is characterized by columnar quartz crystals that grow perpendicularly towards the center and along the two walls of the fissures, indicating open-space filling. The center of the comb structure locally evolves into a drusy/miarolitic structure, which may be filled with pyrite, further reflecting the process of open-space filling in the hypabyssal hydrothermal environment.

The ore textures can be classified into crystalline textures, metasomatic textures, recrystallization textures, and deformation textures. Crystalline textures (Fig. 4a–d) include xenomorphic, euhedral-subhedral, and common-growth textures. The minerals of xenomorphic textures include pyrite, chalcopyrite, and quartz. Minerals of subhedral textures include columnar arsenopyrite and pyrite, and minerals of euhedral texture include cubic pyrite and columnar arsenopyrite. The common-growth textures are found between galena and sphalerite as well as between chalcopyrite and sphalerite. Metasomatic textures (Fig. 4b, 4c, 4e–j) include etching, reaction-

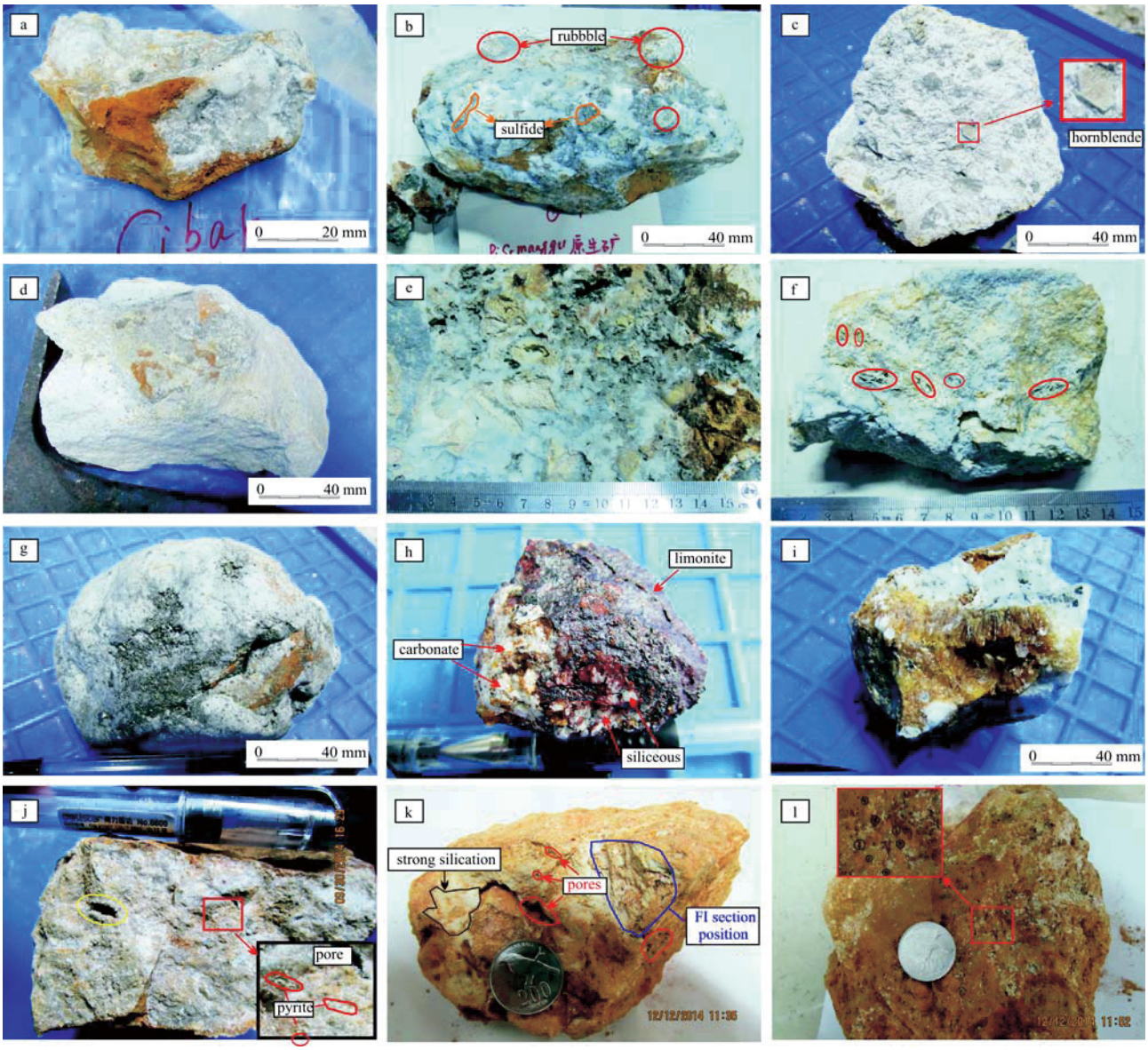

Fig. 3. Ore types and structures.

(a), Massive quartz ore, from Cibak block; (b), Tectonic breccia ore, Pasir Manggu block; (c), Hornblende quartz porphyry ore, Cipirit block; (d), Disseminated pyrite in altered andesite, Pasir Manggu block; (e), Stockwork structure with andesite leaching and clay alteration, and network of quartz veins, Pasir Manggu block; (f), High Au grade vuggy ore with scattered pyrite in siliceous rock, Cibak block; (g), Massive pyrite and arsenopyrite in fractured andesite, Cileuweung block; (h), Carbonatization and ferritization, Cileuweung block; (i), Comb/miarolitic quartz, Cibak block; (j), Chalcedonization ore with pores and scattered sulfides, Cibak block; (k), Structurally controlled alteration ores, Cikadu block; (l), Vuggy siliceous rocks, Cikadu block.

boundary and metasomatic relict textures. Etching textures are characterized by replacing of earlier minerals by the later minerals, including gangue minerals replaced by metallic minerals (e.g., pyrite replacing quartz along the borders) and metallic minerals replaced by the later metallic minerals (e.g., arsenopyrite replacing pyrite, sphalerite replacing pyrite, chalcocite replacing bornite, galena replacing sphalerite, and pyrites of a younger generation replacing older ones). Reaction-boundary textures are characterized by the replacement of a metallic mineral by other minerals around the crystal edges. Metasomatic relict textures consist of pyrite and bornite relicts in arsenopyrite and chalcocite due to the replacement by the latter. Recrystallization textures (Fig. 4k) were formed after mineralization. And deformation textures (Fig. 4l) are characterized by quartz filling the cracks in pyrite.

In Pasir Manggu, where quartz-sulfide vein type ores are developed, three stages of mineralization processes have been identified (Jonathan, 2007). (1) The early stage is characterized by a banded chalcedony–silica, generally without gold mineralization and with little metal sulfidation. (2) The second stage is characterized by the arsenopyrite-arsenic pyrite-quartz veins and brecciation.

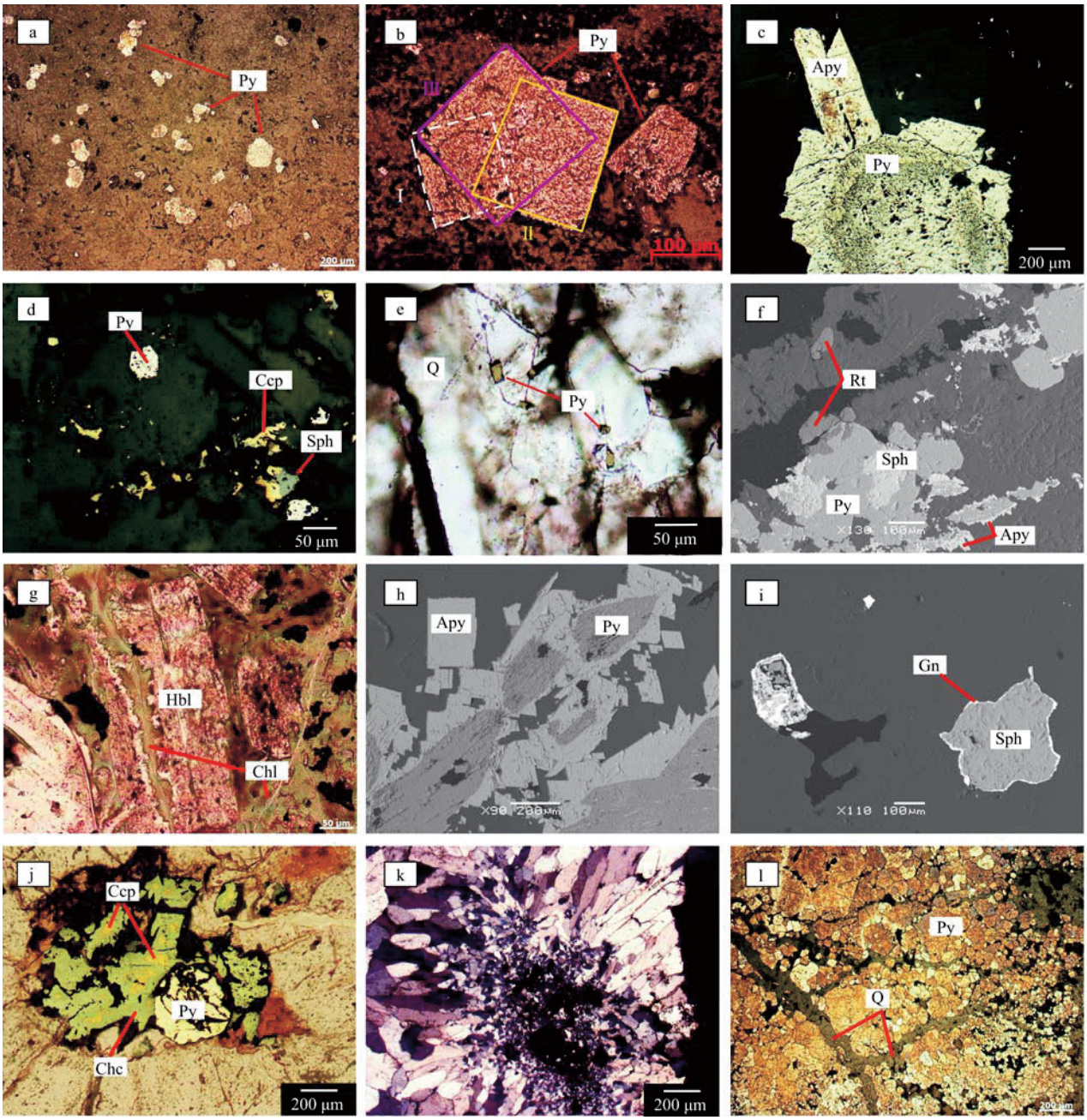

Fig. 4. Ore textures.

(a), Pyrite with xenomorphic-subhedral texture; (b), Pyrite with subhedral-euhedral texture; (c), Metasomatic texture with pyrite replaced by euhedral columnar and granular arsenopyrite; (d), Disseminated chalcopyrite and granular pyrite within quartz; (e), Fine grained euhedral-subhedral pyrite within quartz; (f), Etching texture, with euhedral pyrite replaced by arsenopyrite, BSE image; (g), Hornblende replaced by chlorite; (h), Metasomatic relict texture with xenomorphic pyrite bordered by columnar arsenopyrite, BSE image; (i), Metasomatic texture with sphalerite replaced by arsenopyrite, BSE image; (j), Metasomatic relict texture with chalcopyrite replaced by chalcocite; (k), Quartz with radiating texture; (l), Pyrite with crushed texture.

Py-pyrite, Apy-arsenopyrite, Ccp-chalcopyrite, Sph-sphalerite, Q-quartz, Rt-rutile, Hbl-hornblende, Chl-chlorite, Gn-galena, Bn-bornite, Chc-chalcocite.

The arsenopyrite and arsenic pyrite always contain various amounts of Au. (3) The third stage is characterized by the ore-bearing hydrothermal filling and metasomatism, forming banded structures of chalcedony cement and metal sulfides and intergrowths of large amount of ore minerals. The extensional faults resulted from tectonic activity provide the filling space for this stage (Zhang et al., 2015).

4 Sampling and Analytical Methods

4.1 Sample descriptions

The samples were collected from the quartz-sulfide vein type ores in the Cibak and Pasir Manggu blocks, the porphyry-hosted ores in the Cipirit block, and the structurally controlled alteration type ores in the Cikadu block (sample locations shown in Fig. 2a). The samples

from Pasir Manggu ore block are labeled P1 and P2, the sample from Cipirit is CI, samples from Cibak are C0, C04, C05, C09, and C14, and the sample from Cikadu is Ck2.

The P1 and P2 ores belong to the second mineralization stage: they exhibit breccia structures and display quartz intergrowth with Au-bearing arsenopyrite and arsenic pyrite (Fig. 3b; Fig. 5e–f). The other samples also exhibit mineralization features (Fig. 3k; Fig. 5a–d), although a clear paragenetic sequence has not been established. Features indicating syn-mineralization quartz include the fine grain quartz and chalcedony coexisting with the arsenopyrite in C14 (Fig. 5b), and quartz displaying intergrowth with arsenopyrite, pyrrhotite, chalcocite, chalcopyrite and sphalerite (Fig. 5d).

4.2 Analytical methods of microthermometry and laser Raman spectroscopy

Doubly polished sections of high transparency ore quartz were selected for fluid inclusion study. First, petrographic observations of fluid inclusions were performed using an optical microscope. Then, representative samples containing high quality inclusions were selected for microthermometric measurements and laser Raman spectroscopy analysis. The above laboratory works were completed at the State Key Laboratory of Ore Deposit Geochemistry, Chinese Academy of Sciences. The microthermometry was performed using a Linkam THMSG 600 Hot & Cold Stage with the following technical parameters: temperatures ranging from −196°C to 600°C, and freezing and heating data precisions of ±0.1°C and ±2°C, respectively. Raman spectroscopy for vapor phase of individual fluid inclusions was measured with a Renishaw inVia Reflex Raman spectroscope. Excitation was provided by a Spectra-Physics argon-ion laser at 20mW with a wavelength of 514.5 nm focused to a spot size of 1–2 μm, with a counting time of 60 s or 120 s.

For liquid-rich two-phase inclusions, the homogenization temperatures (Th) were measured by heating the inclusions to the liquid phase (Bakker and Jansen, 1994; Lu Huanzhang et al., 2004). The first melting temperatures are approximately −21° C, suggesting that the salt dissolved in the fluid inclusions is NaCl (Lu Huanzhang et al., 2004). Salinities of liquid-rich fluid inclusions were calculated from the last ice-melting temperatures (T_m) according to the formula of Bodnar (1993). Fluid densities were calculated using the equation of Brown and Lamb (1989) by using the computer program of FLINCOR (Brown, 1989).

4.3 Analytical methods for oxygen and hydrogen isotopes

Seven samples of auriferous quartz were selected from P1, P2, CI, C0, C5, C14, and C15 for hydrogen and oxygen isotope analyses. The quartz samples were crushed to small pieces of 0.25–0.5 mm in size, and quartz grains with purities over 95% were hand-picked under a monocular microscope. Oxygen and hydrogen isotope analyses of quartz were performed at the Laboratory of Metallogency and Mineral Assessment, Chinese Academy of Geological Sciences. The pure quartz was ablated in the presence of BrF_5 reagent to liberate oxygen gas (Clayton et al., 1972). The δD values of water extracted from fluid

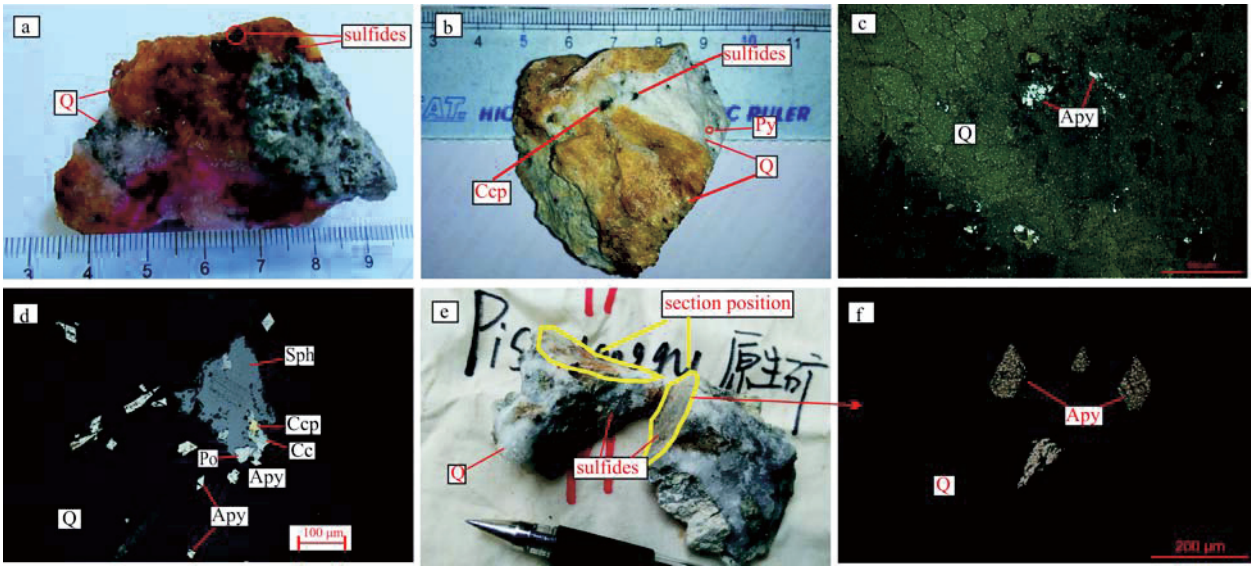

Fig. 5. Photographs showing relationships between the quartz used for study and metallic minerals.
(a), Disseminated polymetallic sulfides in quartz. The red mark near the ruler indicates the location of thin section, from C0; (b), Chalcopyrite, pyrite, and other metallic sulfides intergrown with massive quartz, from C04; (c), Arsenopyrites intergrown with fine-grained quartz and chalcedonic quartz, from C14; (d), Sphalerite, chalcocite, chalcopyrite, pyrrhotite and arsenopyrite coexisting with quartz, from CI; (e), Polymetallic sulfides disseminated in quartz breccia, from P1; (f), Arsenopyrite and quartz aggregating in the second mineralization stage, from P1.
Q-quartz, Py-pyrite, Apy-arsenopyrite, Ccp-chalcopyrite, Sph-sphalerite, Cc-chalcocite, Po- pyrrhotite.

inclusions in quartz were analyzed using the Zn reduction method (Coleman et al., 1982). Both the oxygen and hydrogen isotopes were measured using a MAT253-type mass spectrometer. The results are reported in standard notation, expressed relative to the Vienna Standard Mean Ocean Water (VSMOW). The analytic precision of H_2 is ±1‰, and that of O_2 exceeds ±0.2‰.

Because hydrogen was measured directly from fluid inclusions, the measured δD_{VSMOW} represents the fluid composition. The measured $\delta^{18}O_{VSMOW}$ values were determined from the quartz and can not represent the composition of fluid. $\delta^{18}O_{H2O\text{-}VSMOW}$ values were calculated using the formula of $1000\ln\alpha_{Q\text{-}H2O}=3.38\times10^{-6}T^{-2}-3.4$ (Clayton et al., 1972), where T (in degree K) is the mean homogenization temperature of corresponding fluid inclusions.

5 Analysis Results

5.1 Fluid inclusions petrography and Raman spectroscopy

In general, the petrographic features of the fluid inclusions (FIs) from the quartz-sulfide veins and porphyry-hosted ores are similar. The FIs in strongly silicified samples from Cikadu (structurally controlled alteration ores) are scarce and relatively small in size (Fig. 6k–l). At room temperature, the fluid inclusions can be divided into the vapor-liquid two phase FIs and the single liquid phase FIs (Fig. 6a). The two-phase FIs are dominant and liquid-rich (Fig. 6b), and most are relatively large. By contrast, the single-phase liquid FIs are very rare and small. FIs containing daughter minerals and the double-edged CO_2-bearing FIs were not observed. The liquid percentage in the two-phase FIs ranges from 75% to 90%. The FIs are distributed in clusters (Fig. 6a), isolation (Fig. 6b, 6e), and trails (Fig. 6c) within individual crystals. The absence of trails cutting across the quartz crystals indicates that the inclusions are primary or pseudosecondary. Individual inclusions are irregular or regular (Fig. 6d–g). The regular inclusions exhibit negative crystal shapes (Fig. 6h), or oval (Fig. 6i) or triangular shapes (Fig. 6j). The size of the FIs range from <5 μm to> 35 μm, but most are <15 μm.

According to the shape, size, liquid volume percentage and other physical features, the fluid inclusions can be classified into five types. Type I FIs have the regular shape, size > 13 μm, liquid volume percentage> 80%, clear outline of vapor phase, and they are always isolated or in clusters of three inclusions or less (Fig. 4a, 4e, 4j). Type I fluid inclusions are common and are the main type of inclusions analyzed in this study. Type II FIs have irregular shape, size > 13 μm, liquid volume percentage of 70%–90%, fuzzy outline of the vapor phase, and they are always isolated or in clusters (Fig. 4g–h). Type III FIs have regular shape, size of 5–13 μm, liquid volume percentage >85% mostly, clear or fuzzy outline of the vapor phase, and they are always isolated or in clusters (Fig. 4d, 4i). All FIs from Ck2 sample are of type III (Fig. 4k–l). Type IV FIs have irregular shape, size of 7–15 μm, liquid volume percentage> 85% mostly, fuzzy outline of the vapor phase, and they are always isolated (Fig. 4h). Type V FIs have regular shape, size < 10 μm, high liquid volume percentage (95%–100%), and they are clustered or in trails (Fig. 4a). Type V FIs are too small and may be pseudosecondary or secondary, so they were not analyzed.

Twelve fluid inclusions from samples C0 and P1 with high volumetric contents and large sizes were examined using laser Raman spectroscopy. The strong peak around 3500 cm^{-1} represents the signal of H_2O (Fig. 7a). Visible signals from CO_2 (1285 and 1387 cm^{-1}), N_2 (2331 cm^{-1}), H_2S (2611 cm^{-1}) and CH_4 (2917 and 3020 cm^{-1}) (Frezzotti et al., 2012) were absent from nearly all fluid inclusions. Only one fluid inclusion from sample C0 showed a very weak signal of CO_2 (Fig. 7a).

5.2 Microthermometry

A total of 139 homogenization temperatures (Th) of FIs were measured from quartz-sulfide vein samples (samples C0, C04, C05, C09, C14, P1, and P2). The determined values range from 147°C to 447°C (with a gap between 360°C and 380°C), with an average of 289.2°C. Below 360° C, the Th data have peaks of 280° C–320° C. Homogenization temperatures for 33 inclusions were measured from the porphyry-hosted type ore (sample CI), with values in the range of 239°C–333°C (except for one outlier at 435°C), with an average of 293.6°C, and values concentrated in the 260° C–320° C. Homogenization temperatures for 8 inclusions were measured from structurally controlled alteration ore (sample Ck2), with values of 148°C–326°C, an average of 212.2°C, and seven values occurring in the range of 148°C– 256°C (Table 1).

Generally, the variation of the salinities of FIs is relatively small among the three ore types. For quartz-sulfide vein ores, the final ice-melting temperatures ($T_{m\text{-}ice}$) of FIs are between −13.5 and −7.2°C, with corresponding salinities of 10.7wt%–17.7wt% NaCl equiv (Table 1). For porphyry-hosted ores, the $T_{m\text{-}ice}$ values of FIs are between −14.0 and −10.9°C, with corresponding salinities of 14.9wt%–17.8wt% NaCl equiv (Table 1). The only measured $T_{m\text{-}ice}$ value from Ck2 is −7.5°C, with a corresponding salinity of 11.1wt% NaCl equiv (Table 1). As a whole, the values are concentrated in the range of 14.0wt%–17.0wt% NaCl equiv, indicating a moderate salinity range.

For all samples, the calculated densities of FIs are of 0.646–0.999 g/cm^3, and most of them are concentrated in

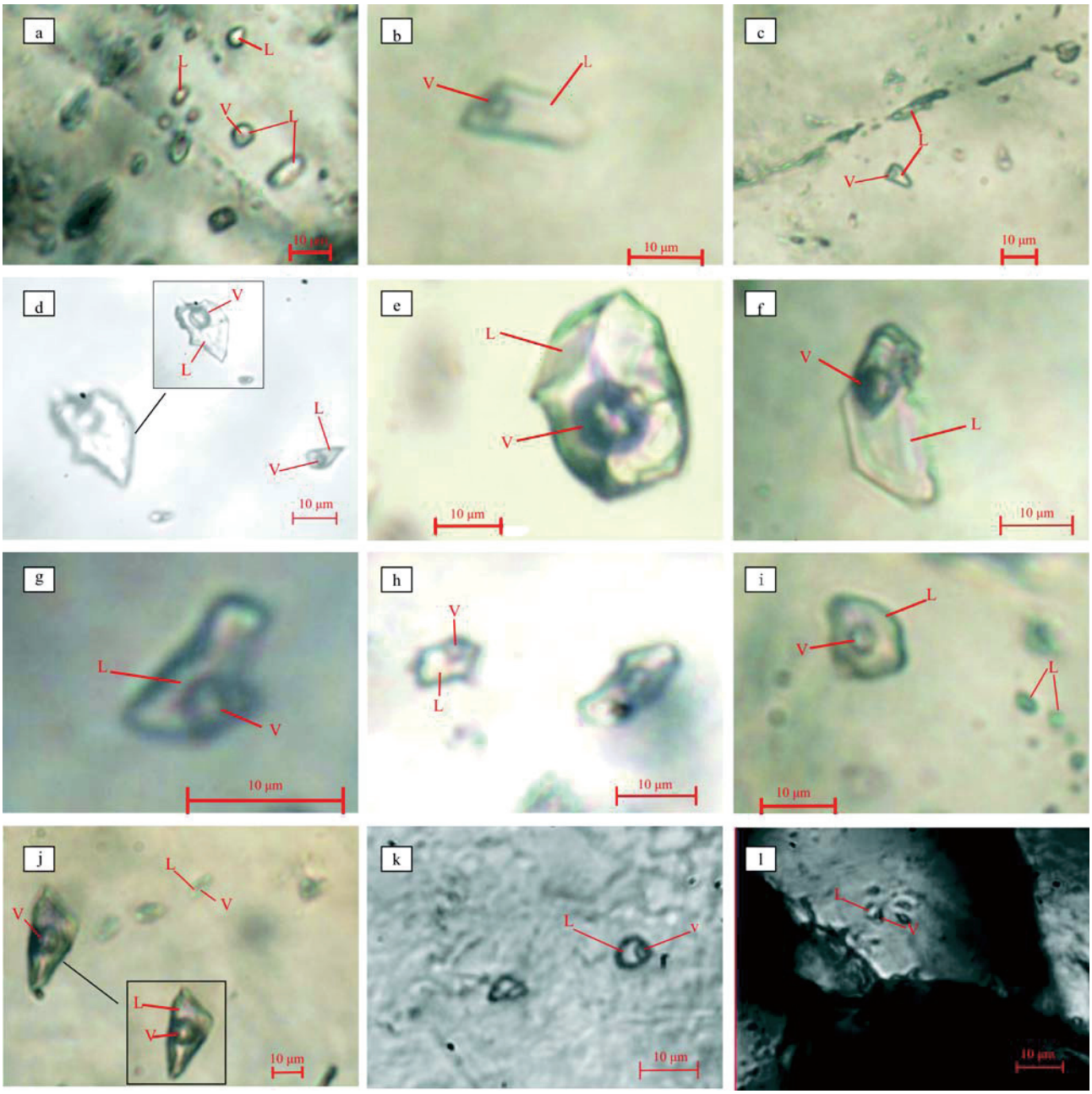

Fig. 6. Micrographs of fluid inclusions.
(a), Coexistence of single liquid phase and liquid-vapor inclusions, from C09; (b), A liquid-rich two phase inclusion, from C04; (c), Linearly distributed inclusions, from C05; (d), Coexistence of two fluid inclusions of different sizes, from P1; (e), An isolated large regular fluid inclusion, from CI; (f), A large irregular inclusion, from CI; (g), A small irregular inclusion, from CI; (h), A small negative crystal inclusion (left), from P1; (i), An ovate fluid inclusion, from C05; (j), A cluster of inclusions (primary or pseudosecondary), from C04; (k), Small regular fluid inclusions, from Ck2; (l), Small fluid inclusions at the edge of non-crystalline SiO_2, from Ck2. L represents liquid, V represents vapor.

the range of 0.85–0.95 g/cm^3. Values below 0.850 g/cm^3 only occur in the quartz-sulfide vein type samples from Cibak block (Table 1). For quartz-sulfide vein ores, the densities of FIs are 0.646–0.999 g/cm^3. For porphyry-hosted samples, the densities of FIs are 0.897–0.947 g/cm^3. The only one measured from Ck2 is 0.951 g/cm^3.

5.3 Oxygen - hydrogen isotope compositions

The $\delta^{18}O_{Q\text{-}VSMOW}$ values for quartz are between +12.9‰ and +14.5‰, and the corresponding values of $\delta^{18}O_{H2O\text{-}VSMOW}$ values for water in equilibrium with quartz are between +5.5‰ and +7.7‰ (Table 2). The δD_{VSMOW} values range from −69‰ to −115‰ (Table 2). The variation in oxygen isotope compositions among quartz-sulfide veins is small (+5.5‰ to +7.7‰), and there is little difference between the quartz-sulfide vein type samples (+5.5‰ to +7.7‰) and the porphyry-hosted type sample (+6.4‰). The δD_{VSMOW} values show a relatively large

Table 1 Microthermometric result of fluid inclusions for quartz in the Ciemas gold deposit

Sample No.	Size of inclusions (μm)	Liquid content (%)	Homogenization temperature (°C)		Final ice-melting temperature (°C)	Salinity (wt% NaCl)		Fluid density (g/cm^3)	Ore type
			range	Average (quantity)		range	Average (quantity)		
C1	4–33	76–96	238–333, 450	293.6(33)	−14.0–−10.9	14.87–17.79	16.13(11)	0.897–0.947	limonitization quartzite
P1	3–41	80–96	231–313	274.9(20)	−13.5–−11.5	15.47–17.34	16.32(12)	0.874–0.961	breccia ore
P2	3–43	76–92	285–351, 425	303.3(16)	−13.5–−10.9	14.87–17.34	15.87(10)	0.876–0.914	breccia ore
C0	4–36	78–95	194–354	277.8(24)	−11.4–−7.2	10.73–15.37	12.95(17)	0.792–0.985	pyritization quartzite
C04	3–35	85–97	147 ~311, 345, 411	264.1(19)	−12.7–−7.3	10.86–16.62	13.78(13)	0.646–0.999	pyritization quartzite
C05	3–28	75–93	256–309, 382(2), 432	304.2(20)	−13.9–−11.5	15.47–17.70	16.26(14)	0.702–0.934	pyritization quartzite
C09	4–28	60–97	168–323, 447	299.6(24)	−13.0–−8.9	12.73–16.89	14.96(15)	0.676–0.972	altered dacite
C14	3–28	80–96	247–347	294.9(17)	−12.2–−10.4	14.36–16.15	15.23(10)	0.859–0.935	pyritization quartzite
Ck2	<4–12	80–95	148–326	212.2(8)	−7.5	11.10	11.10(1)	0.951	siliceous ore

range and are heavily negative. The quartz δD_{VSMOW} values for quartz-sulfide vein range from −70‰ to −115‰, with an average of −85.3‰, and the δD_{VSMOW} values for porphyry-hosted type is −69‰ (Fig. 8, Table 2).

6 Discussions

6.1 Environment of epithermal mineralization

The ore textures and ore structures can provide certain information about the mineralization environment. The presence of comb structures and drusy/miarolitic structures (Fig. 3i) indicate the open-space filling of the near-surface environment, in which hornblende were replaced by chlorite (Fig. 4g), reflecting the activity of low temperature hydrothermal fluid. The combined features of open-space filling, chalcedonic quartz, vuggy quartz, and breccias are common in Ciemas, and they are distinct features of epithermal ore deposits (Chen et al., 2012).

The fluid inclusions retain ancient ore-forming fluids in the minerals and provide the direct evidence of the characteristics of the ore-forming fluids (Lu Huanzhang et al., 2004; Chi Guoxiang and Lai Jianqing, 2009; Mernagh, 2015). Without petrographic judgment on the FIs, the microthermometric analysis may be invalid (Goldstein and Reynolds, 1994; Chi Guoxiang and Lu Huanzhang, 2008). In Ciemas, the T*h* differences between neighboring FIs are always below 30°C. Most T*h* values of Type I FIs are between 280°C and 320°C, and only two produce values of 382°C (Table 1, Fig. 7c). The T*h* values of type II inclusions vary greatly, and are concentrated in the range 260–320 °C, while a very few are much higher (>400°C). Those inclusions beyond 400°C have very irregular shapes and may have been modified by later activity, thus they are invalid and should be disregarded (Chi Guoxiang and Lu Huanzhang, 2008). The T*h* values of type III inclusions are scattered, with most lying below 320°C. The T*h* values of type IV inclusions range from 240°C to 320°C (Fig. 7c). Type V fluid inclusions may include secondary inclusions and are too small to measure, therefore, they were not analyzed. For the quartz-sulfide vein and porphyry-hosted ores, most homogenization temperatures of the fluid inclusions are in the moderate temperature range. The structurally controlled alteration type exhibits lower homogenization temperatures because they are relatively far from the dacite and porphyry body (Fig. 2a). The variation in salinities is relatively small, no matter which kind of classification is considered.

Homogenization temperatures for all three ore types are mainly below 320°C (Fig. 7d; Table 1), with moderate salinities (14.0wt%–17.0wt% NaCl equiv). Likewise, the petrographic characteristics of fluid inclusions (liquid-rich two-phase, no daughter minerals, no or little CO_2) are

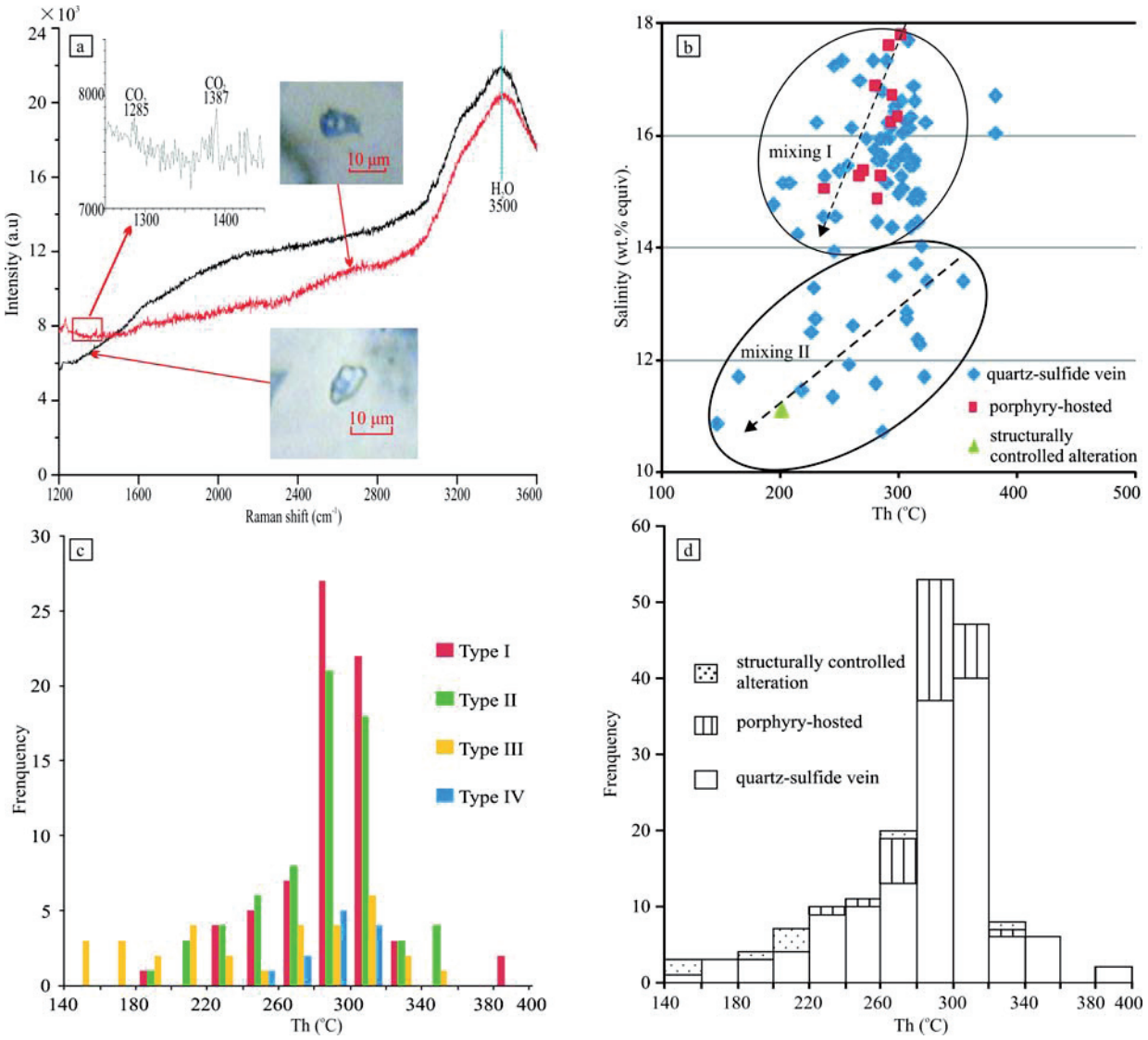

Fig. 7. (a), Laser Raman spectra of the vapor phase in individual fluid inclusions. The red line (from sample C0) shows a very weak CO_2 signal while the black one (from P1) has no signal for common gas composition. Both spectra have a strong H_2O peak around 3500 cm^{-1}. (b), T*h* versus salinity diagram showing two mixing trends. (c), Histogram of valid homogenization temperatures for different fluid inclusion types. (d), Histogram of valid homogenization temperatures for different ore types.

Table 2 Hydrogen and oxygen isotope compositions of quartz in Ciemas gold deposit

Sample No.	δD_{VSMOW} (‰)	$\delta^{18}O_{Q\text{-}VSMOW}$ (‰)	Mean Th (°C)	$\delta^{18}O_{H2O\text{-}VSMOW}$ (‰)
P1	−85	+13.9	274.9	+6.0
P2	−115	+14.5	303.3	+7.7
C0	−88	+13.2	277.8	+5.5
C5	−69	+13.3	304.2	+6.6
C14	−85	+13.5	294.9	+6.4
C15	−70	+12.9	299.6	+6.0
CI	−69	+13.7	289.2	+6.4

consistent with those of typical epithermal gold deposits (Hedenquist et al., 2000; Chen Yanjing et al., 2007) and those of other epithermal gold deposits in West Java (Marcoux and Milési, 1994; Warmada et al., 2007; Yuningsih et al., 2014). In addition, the host rocks of Ciemas are early Miocene (17.1–17.5 Ma) calk-alkaline igneous rocks formed in the subduction setting (Zhang et al., 2015). Such calk-alkaline host rocks, including volcanic breccia, dacite, and andesite, are common in the epithermal deposits (Cooke and Simmons, 2000; Chen et al., 2012). All of the above suggests that Ciemas is an epithermal gold deposit associated with porphyry (White and Hedenquist, 1995; Sillitoe, 1997).

6.2 Water sources

The $\delta^{34}S$ values of +4.90 to +6.99‰ for pyrite of ore

rocks in Ciemas are similar to those of the lavas (+3.2 to +4.5‰) (Krakatau and Guntur) in the western Sunda arc (De Hoog et al., 2001), indicating the incorporation of magmatic sulfur into the epithermal fluid system in Ciemas (Zheng Chaofei et al., 2014). The fluid inclusion homogenization temperatures and salinities in Ciemas are also consistent with the magmatic derivation of fluids (Tran Mydung et al., 2016). Epithermal precious deposits generally have combined fluid compositions of magmatic hydrothermal fluids and meteoric water (Hedenquist and Lowenstern, 1994). Meteoric water accounts for the major proportion in most low sulfidation mineralization (Zhai Wei et al., 2007; Chen et al., 2012). On account of most FIs in the ores being primary or pseudosecondary in Ciemas, the oxygen-hydrogen isotope data can be used to determine the water sources. The δD values (−69 to −88‰, −115‰) for quartz in Ciemas are much lower than those of the modern meteoric water in West Java (rivers and hot springs showing δD in the range of −32 to −51‰) (Yuningsih and Matsueda, 2014) (Fig. 8). In addition, the $\delta^{18}O_{H2O}$ values (+5.5 to +7.7‰) are much higher than those of modern meteoric water and are close to the values of degassed magma (Hedenquist and Lowenstern, 1994) (Fig. 8).

Magmatic hydrothermal fluids can often oxygen-shifted but are rarely hydrogen-shifted as a result of water-rock interaction (Hedenquist and Lowenstern, 1994). During the evaporation of water, the light isotopes largely enter the vapor phase, whereas the heavy isotopes stay behind largely (Clayton et al., 1972). This supports the finding that the values of δD and δ^{18}O in fluid inclusions and speleothem calcite show an increasing trend with age from older to modern in West Java (Griffiths et al., 2010). Thus, the local paleo-meteoric water at the time of Ciemas ore deposition should have had significantly lower δD values than those of the present (Fig. 8). The same interpretation

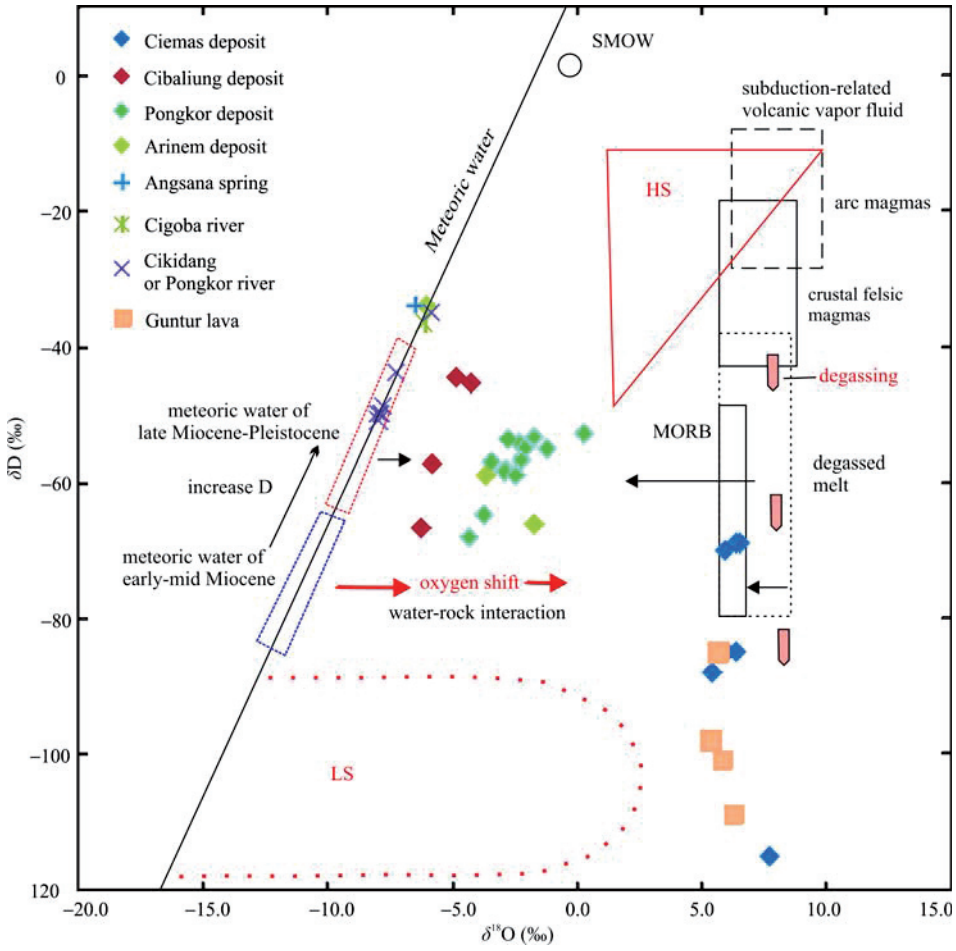

Fig. 8. Plot of δD versus δ^{18}O for fluids from Ciemas, neighboring rivers and other gold deposits in West Java.

The values of δD and δ^{18}O values for paleo-meteoric water are lower than those of modern water. The magmatic fluids have lower δD than primary magma due to degassing, and the elevated δ^{18}O for water results from water-rock interaction. The base diagram is after Hedenquist and Loewenstern (1994).Data from other localities including the Cibaliung deposit, the Cigoba river (Harijoko et al., 2007), the Pongkor deposit (Imai and Watanabe, 2007), the Arinem deposit, the Angsana spring, the Pongkor river, the Cikidang river (Yuningsih and Matsueda, 2014), and the Guntur lava (De Hoog et al., 2009) are also shown for comparison. LS= low sulfidation, HS= high sulfidation.

was applied at the Sahinli epithermal deposit in Turkey (Yilmaz et al., 2010). The δD and δ^{18}O values for quartz in Ciemas match those of the lava flow from Guntur area and Krakatau volcano (δD_{SMOW} of −85 to −109‰, $\delta^{18}O_{SMOW}$ of +5.4 to +6.3‰) in West Java (De Hoog et al., 2009). Hence the primary magmatic hydrothermal ore-forming fluid should be plotted to the right of the Guntur data in Fig. 8. Therefore, it is proposed that the ore-forming fluids are the mixtures of the lower δD and δ^{18}O paleo-meteoric water and degassed magmatic hydrothermal fluid, in which the magmatic water is dominant. Because of the shortage of hydrogen isotope analysis method, the δD (based on water extracted from fluid inclusions) may reflect the combined information from five types FIs. The fluid inclusions of type V may include secondary inclusions, and they are very small and have higher liquid percentage, thus, they may be formed in a lower temperature environment and contain more meteoric water. However, the secondary FIs are minor, so the actual water sources are still the mixing of large amounts of magma-derived fluids and meteoric water.

6.3 Deposition mechanism

According to the petrography of fluid inclusions, there is no obvious evidence of boiling because of no coexistence of vapor-rich inclusions with liquid-rich inclusions (Brown, 1986; White and Hedenquist, 1995). Remarkably, the positive correlation between homogenization temperatures and salinities over a broad range indicates mixing as the main mechanism for mineral precipitation (Fig. 7b) (Wilkinson, 2001; Canet et al., 2011).

A descriptive geological–metallogenic model in Ciemas has been proposed (Zhang et al., 2015). In this paper, the ore deposition mechanism based on inclusion data is emphasized. Base on a schematic model of ore precipitation consistent with the relationship between homogenization temperatures and salinities (Hedenquist and Henley, 1985; Wilkinson, 2001; Canet et al., 2011), the ore precipitation in Ciemas is revealed as follows (Fig. 7b):

During the Early Miocene, an important episode of volcanism took place in south Java as a result of northward subduction of the Indio-Australia underneath the Eurasian plate, which led to the development of a system of caldera structures (Fig. 1) (Clements and Hall, 2007). Andesite, dacite, and quartz diorite porphyry were generated in sequence. Faults and fractures were simultaneously generated that became important sites for later mineralization (Zhang et al., 2015). In the hydrothermal fluid mineralization stage, two mixing processes may have occurred. The first mixing event (termed mixing I here) occurred in quartz-sulfide vein and porphyry-hosted type ore blocks (Fig. 7b), in which the magma-derived hydrothermal fluid mixed with the paleo-meteoric water. A sharp decrease in both T*h* and salinity (T*h* from ~340°C to ~180°C, salinity from ~18% to ~14 wt% NaCl equiv) resulted in large amounts of quartz-gold-sulfides deposition in the porphyry bodies and contact zones. After mixing I, the residual mixed ore fluids were transported to distant spaces and mixed with the paleo-meteoric water (termed mixing II), resulting in further decreases in both T*h* and salinity (accompanied with Au deposition). However, the descent of salinity is slower (Fig. 7b) than first mixing because the salinity gap between the two kinds of fluids was smaller. If the mixing II took place in a fault zone which caused rock crushing, the structurally controlled altered gold bodies would be formed. Notably, cooling was ongoing during the entire process of hydrothermal fluid activity and contributed to the mineral deposition. Combining with the H-O isotopic data, the mixing of large amounts of magmatic hydrothermal fluids with the meteoric water is the main ore deposition mechanism in the Ciemas gold deposit.

6.4 Comparisons with other epithermal deposits in West Java

The homogenization temperature and salinity values of FIs in Ciemas are relatively higher than those of other epithermal deposits in West Java (Milesi et al., 1994; Milesi et al., 1999) (Fig. 9) and those of typical epithermal precious deposits (Cooke and Simmons, 2000; Chen Yanjing et al., 2007). The acidic ore fluid reflected by leaching structures(e.g., vuggy quartz), the considerable magmatic-derived water composition, and the precipitation mechanism of mixing are all consistent with previous research results (Chen Yanjing et al., 2007; Zhang et al., 2015), which demonstrate that the Ciemas mineralization is of high sulfidation mineralization associated with porphyry.

In West Java, the biggest known age difference between ore mineralization (K-Ar dating on adularia of 1.7 Ma) and the igneous host rock (microdiorite of 4.5 Ma) (Milesi et al., 1994) is 2.8 Ma (occurs in the Cirotan deposit). The youngest host rock age in Ciemas was determined in an amphibolite tuff breccia of 17.1 Ma (zircon U-Pb dating) (Wu et al., 2014), so a reasonable mineralization age might be ~14.3Ma (middle Miocene). Thus, the Ciemas gold deposit could be the oldest epithermal deposit in West Java. In the literatures of the epithermal deposits in West Java (Marcoux and Milési, 1994; Milesi et al., 1994; Rosana and Matsueda, 2002; Imai and Watanabe, 2007; Warmada et al., 2007; Yuningsih et al., 2012; Yuningsih et al., 2014), some similarities and differences of their ore fluid features are summarized. For the epithermal precious deposits (with or without base metals) in West Java,

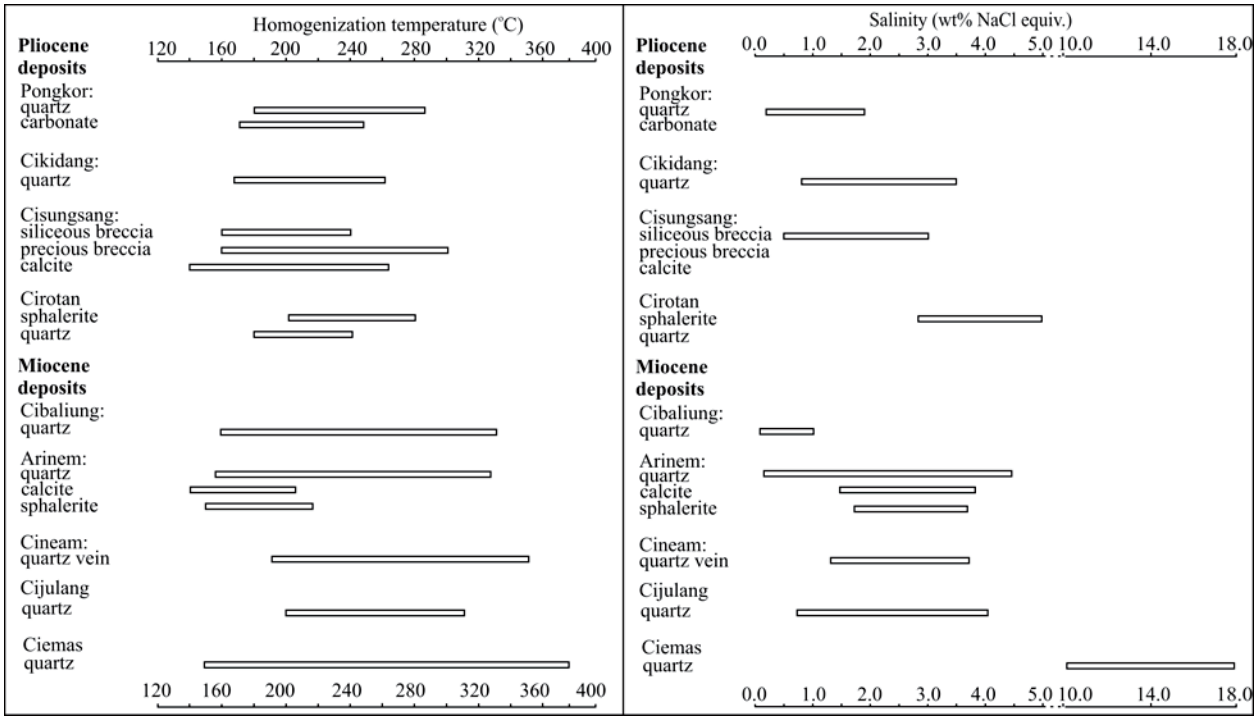

Fig. 9. Homogenization temperatures and salinities of fluid inclusions from epithermal precious metal deposits in West Java. Published data from (Marcoux and Milési, 1994; Milesi et al., 1999; Harijoko et al., 2007; Yuningsih et al., 2012; Tun et al., 2014a; Yuningsih et al., 2014).

nearly all of the fluid inclusions in quartz, calcite, and sphalerite are simple aqueous inclusions, and most have high liquid volume percentages (>70%).

The Miocene deposits have slightly higher fluid inclusion homogenization temperatures than those of Pliocene–Pleistocene (Fig. 9). The salinity values of Miocene deposits are also higher than those of most Pliocene–Pleistocene deposits except for Cirotan (Fig. 9). Among the Pliocene–Pleistocene deposits, the Cirotan deposit contains abundant sulfides, whereas Pongkor and Cikidang are poor in sulfides. The Miocene ore deposits are always abundant in sulfides, and always contain enargite (in Cijulang) which is a typical high sulfidation metallic mineral. No H-O isotope data for quartz or calcite from deposits of West Java are plotted in typical low sulfidation or high sulfidation zones based on the base map of Hedenquist and Lowenstern (1994) (Fig. 8), but they display some genetic features and trends. As discussed above, the older paleo-meteoric water has relatively low δD values. Ore-forming fluids are rich in the meteoric water in the young LS deposits of Pongkor (Imai and Watanabe, 2007), Cibaliung (Harijoko et al., 2007), while the old HS deposit of Ciemas is rich in magmatic-derived water. In the two sets of H-O isotope data in Arinem, one set plots close to the meteoric water line, and the other lies far away from meteoric water line and approaches to the magmatic-derived field. This can be explained by that the high sulfidation mineralization overprinting the low sulfidation mineralization in Arinem (Yuningsih and Matsueda, 2014). The higher T*h* and salinities of FIs and greater amount of magmatic derived water in Ciemas are associated with the Cipirit porphyry magma, suggesting a close spatial and temporal relationship to Early Miocene volcanism (Clements and Hall, 2007).

7 Conclusions

(1) Fluid inclusions in quartz from the quartz-sulfide vein and porphyry-hosted ore blocks are liquid-rich two-phase inclusions that have moderate to high homogenization temperatures (240–320°C) and moderate salinities (14–17 wt% NaCl equiv). Fluid inclusions from structurally controlled alteration ore block exhibit low T*h* and salinities because they are far from the porphyry body.

(2) Mixing and cooling contributed to the precipitation of quartz-sulfide-gold in Ciemas, in which the greater contribution comes from the mixing of large amounts of magma-derived fluid with meteoric water. Fluid inclusions data, hydrogen and oxygen isotope compositions and ore structures and textures indicate that Ciemas is an epithermal gold deposit associated with porphyry.

(3) Early Miocene volcanic activities produced high sulfidation, combined high sulfidation–low sulfidation and

minor low sulfidation mineralization in the southernmost part of West Java. Late Miocene–Pliocene volcanic activities produced significant low sulfidation mineralization in the south-central part of West Java, farther from the Sunda trench. The former contains more material and heat sourced from the magma than the latter due to the spatial and temporal differences in relation to the subduction zone.

Acknowledgments

This research is financially supported by the National Natural Science Foundation of China (NFSC No. 41573039). We are grateful to Prof. Zhou Meifu of Hongkong University and Prof. Lu Huanzhang of Quebec University for their helpful suggestions for this study. Also, we thank Prof. Guoxiang Chi (Associate Editor-in-Chief) and two anonymous reviewers so much for their careful reviews and constructive suggestions, which helped us to improve our manuscript.

Manuscript received Mar. 17, 2016
accepted Sept, 24, 2016
edited by Fei Hongcai

References

Bakker, R.J., and Jansen, J.B.H, 1994. A mechanism for preferential H_2O leakage from fluid inclusions in quartz, based on TEM observations. *Contributions to Mineralogy and Petrology*, 116(1): 7–20.

Bodnar, R., 1993. Revised equation and table for determining the freezing point depression of H_2O-NaCl solution, *Geochim Cosmoehim Acta*, 57: 683–684.

Brown, K.L., 1986. Gold deposition from geothermal discharges in New Zealand. *Economic Geology*, 81(4): 979–983.

Brown, P.E., 1989. FLINCOR: a microcomputer program for the reduction and investigation of fluid-inclusion data. *American Mineralogist,* 74(11–12): 1390–1393.

Brown, P.E., and Lamb, W.M., 1989. P- V- T properties of fluids in the system H_2O±CO_2±NaCl: New graphical presentations and implications for fluid inclusion studies. *Geochimica et Cosmochimica Acta,* 53(6): 1209–1221.

Canet, C., Franco, S.I., Prol-Ledesma, R.M., González-Partida, E., and Villanueva-Estrada, R.E., 2011. A model of boiling for fluid inclusion studies: Application to the Bolaños Ag–Au–Pb–Zn epithermal deposit, Western Mexico. *Journal of Geochemical Exploration,* 110(2): 118–125.

Chen Yanjing, Ni Pei, Fan Hongrui, Pirajno, F., Lai Yong, Su Wenchao and Zhang Hui, 2007. Diagnostic fluid inclusions of different types hydrothermal gold deposits. *Acta Petrologica Sinica,* 23(9): 2085–2108 (in Chinese with English abstract).

Chen, Y.J, Pirajno, F., Wu, G., Qi, J., and Xiong, X., 2012. Epithermal deposits in north Xinjiang, NW China. *International Journal of Earth Sciences,* 101(4): 889–917.

Chi Guoxiang and Lu Huanzhang. 2008. Validation and representation of fluid inclusion microthermometric data using the fluid inclusion assemblage (FIA) concept. *Acta Petrologica Sinica*, 24(9): 1945–1953.

Chi Guoxiang and Lai Jianqing, 2009. Roles of fluid inclusions in study of mineral deposits. *Mineralium Deposita*, 28: 850–855 (in Chinese with English abstrac).

Clayton, R.N., O'Neil, J.R., and Mayeda, T.K., 1972. Oxygen isotope exchange between quartz and water, *Journal of Geophysical Research,* 77(17): 3057–3067.

Clements, B., and Hall, R., 2007. Cretaceous to Late Miocene stratigraphic and tectonic evolution of West Java. In: *31st Annual Convention and Exhibition 2007*. Proceedings Indonesian Petroleum Association, 1–18.

Coleman, M.L., Shepherd, T.J., Durham, J.J., Rouse, J.E., and Moore, G.R., 1982. Reduction of water with zinc for hydrogen isotope analysis. *Analytical Chemistry*, 54(6): 993–995.

Cooke, D.R., and Simmons, S.F., 2000. Characteristics and genesis of epithermal gold deposits. *Reviews in Economic Geology*, 13: 221–244.

De Hoog, J., Taylor, B., and Van Bergen, M., 2001. Sulfur isotope systematics of basaltic lavas from Indonesia: implications for the sulfur cycle in subduction zones. *Earth and Planetary Science Letters,* 189(3): 237–252.

De Hoog, J.C., Taylor, B.E., and Van Bergen, M. J., 2009. Hydrogen-isotope systematics in degassing basaltic magma and application to Indonesian arc basalts. *Chemical Geology,* 266(3): 256–266.

Frezzotti, M.L., Tecce, F., and Casagli, A., 2012. Raman spectroscopy for fluid inclusion analysis, *Journal of Geochemical Exploration,* 112: 1–20.

Goldstein, R.H., and Reynolds, T.J., 1994. Systematics of fluid inclusions in diagenetic minerals. *SEPM Short Course*, 31: 199 .

Griffiths, M.L., Drysdale, R.N., Vonhof, H.B., Gagan, M.K., Zhao, J.X., Ayliffe, L.K., Hantoro, W.S., Hellstrom, J.C., Cartwright, I., and Frisia, S., 2010. Younger Dryas–Holocene temperature and rainfall history of southern Indonesia from $\delta^{18}O$ in speleothem calcite and fluid inclusions. *Earth and Planetary Science Letters,* 295(1): 30–36.

Harijoko, A., Ohbuchi, Y., Motomura, Y., Imai, A., and Watanabe, K., 2007. Characteristics of the Cibaliung gold deposit: Miocene low‐sulfidation‐type epithermal gold deposit in Western Java, Indonesia. *Resource Geology*, 57(2): 114–123.

Harijoko, A., Sanematsu, K., Duncan, R. A., Prihatmoko, S., and Watanabe, K., 2004. Timing of the mineralization and volcanism at Cibaliung gold deposit, Western Java, Indonesia. *Resource Geology,* 54(2): 187–195.

Hedenquist, J.W., Arribas, A., and Gonzalez-Urien, E., 2000. Exploration for epithermal gold deposits. *Reviews in Economic Geology*, 13(2): 45–77.

Hedenquist, J.W., and Henley, R.W., 1985. The importance of CO_2 on freezing point measurements of fluid inclusions; evidence from active geothermal systems and implications for epithermal ore deposition. *Economic Geology*, 80(5): 1379–1406.

Hedenquist, J.W., and Lowenstern, J.B., 1994. The role of magmas in the formation of hydrothermal ore deposits. *Nature*, 370: 519–527.

Gao, H., Hu, F.L., Hu, M.H., Richard, K., Li, Y.H., and Xie, P.F., 2013. *Independent qualified Person's Report for the Ciemas gold project, Ciemas, Sukabumi Region, Republic of Indonesia* (Project Number: SHK191), Jakarta.

Imai, A., and Watanabe, K., 2007. Origin of ore-forming Fluids Responsible for gold mineralization of the Pongkor Au‐Ag Deposit, West Java, Indonesia: Evidence from Mineralogic, Fluid Inclusion Microthermometry and Stable Isotope Study of the Ciurug–Cikoret Veins. *Resource Geology,* 57(2): 136–148.

Jonathan, M.N., 2007. *Ciemas prospect West Java, Indonesia geological evaluation study*. Jakarta: Geological Report, 46.

Lu Huanzhang, Fan Hongrui, Ni Pei, Ou Guangxi, Shen Kun and Zhang Wenhuai, 2004. *Fluid Inclusions*. Beijing, Science Press, 484 (in Chinese).

Marcoux, E., and Milési, J.-P., 1994. Epithermal gold deposits in West Java, Indonesia: geology, age and crustal source. *Journal of Geochemical Exploration*, 50(1): 393–408.

Mernagh, T.P., 2015. A review of Fluid inclusions in diagenetic systems. *Acta Geologica Sinica* (English Edition), 89(3): 697–714.

Milesi, J., Marcoux, E., Nehlig, P., Sunarya, Y., Sukandar, A., and Felenc, J., 1994. Cirotan, West Java, Indonesia; a 1.7 Ma hybrid epithermal Au-Ag-Sn-W deposit. *Economic Geology*, 89(2): 227–245.

Milesi, J., Marcoux, E., Sitorus, T., Simandjuntak, M., Leroy, J., and Bailly, L., 1999. Pongkor (west Java, Indonesia): a pliocene supergene-enriched epithermal Au-Ag-(Mn) deposit. *Mineralium Deposita,* 34(2): 131–149.

Rosana, M.F., and Matsueda, H., 2002. Cikidang hydrothermal gold deposit in Western Java, Indonesia. *Resource Geology,* 52 (4): 341–352.

Sillitoe, R., 1997. Characteristics and controls of the largest porphyry copper‐gold and epithermal gold deposits in the circum‐Pacific region. *Australian Journal of Earth Sciences,* 44(3): 373–388.

Soeria-Atmadja, R., Maury, R., Bellon, H., Pringgoprawiro, H., Polve, M., and Priadi, B., 1994. Tertiary magmatic belts in Java. *Journal of Southeast Asian Earth Sciences,* 9(1): 13–27.

Sukamto, R., 1975. *Geologic map of the Jampang and Balekambang quadrangles, Java*(Quadrangles 9–XIV–A, 8–XIV–C): Scale 1:100,000, Geological research and development centre, Bandung.

Tran Mydung, Liu Junlai, Li Xiaochun and Dang Mycung. 2016. Geology, Fluid inclusion and isotopic study of the Neoproterozoic Suoi Thau copper deposit, Northwest Vietnam. *Acta Geologica Sinica* (English Edition), 90(3): 913–927.

Tun, M. M., Warmada, I. W., Idrus, A., Harijoko, A., Verdiansyah, O., and Watanabe, K., 2014a. Fluid inclusion studies of the cijulang high-sulfidation epithermal prospect, West Java, Indonesia. *3rd International Conference on Geological and Environmental Sciences* (ICGES), 73: 6–7.

Tun, M.M., Warmada, I.W., Idrus, A., Harijoko, A., Verdiansyah, O., and Watanabe, K., 2014b. High sulfidation epithermal mineralization and ore mineral assemblages of Cijulang prospect, West Java, Indonesia. *Journal of Southeast Asian Applied Geology,* 6(1): 29–38.

Wakita, K., 2000. Cretaceous accretionary–collision complexes in central Indonesia. *Journal of Asian Earth Sciences*, 18(6): 739–749.

Wang Chengshu, 2002. Active subduction and collision in Southeast Asia. *Sedimentary Geology and Tethyan Geology*, 22(1): 92–112 (in Chinese with English abstract).

Warmada, I.W., Lehmann, B., Simandjuntak, M., and Hemes, H. S., 2007. Fluid inclusion, rare‐earth element and stable isotope study of carbonate minerals from the Pongkor epithermal gold–silver deposit, West Java, Indonesia, *Resource Geology,* 57(2): 124–135.

White, N.C., and Hedenquist, J. W., 1995. Epithermal gold deposits: styles, characteristics and exploration. *SEG Newsletter,* 23(1): 9–13.

Wilkinson, J., 2001. Fluid inclusions in hydrothermal ore deposits. *Lithos,* 55(1): 229–272.

Wu, C.Q, Zhang, Z.W, Zheng, C.F, and Yao, J.H, 2014. Mid-Miocene (~ 17 Ma) quartz diorite porphyry in Ciemas, West Java, Indonesia, and its geological significance. *International Geology Review,* 57: 1294–1304.

Yilmaz, H., Oyman, T., Sonmez, F.N., Arehart, G.B., and Billor, Z., 2010. Intermediate sulfidation epithermal gold-base metal deposits in Tertiary subaerial volcanic rocks, Sahinli/Tespih Dere (Lapseki/Western Turkey). *Ore Geology Reviews*, 37(3): 236–258.

Yuningsih, E.T., and Matsueda, H., 2014. Genesis and origin of Te–bearing gold–silver–base metal mineralization of the Arinem deposit in western Java, Indonesia, *Journal of Mineralogical and Petrological Sciences,* 109(2): 49–61.

Yuningsih, E.T., Matsueda, H., and Rosana, M.F., 2014. Epithermal gold-silver deposits in western Java, Indonesia: Gold-Silver Selenide-Telluride Mineralization. *Indonesian Journal on Geoscience*, 1(2): 71–81.

Yuningsih, E.T., Matsueda, H., Setyaraharja, E.P., and Rosana, M.F., 2012. The Arinem Te-bearing gold-silver-base metal deposit, West Java, Indonesia. *Resource Geology*, 62(2): 140–158.

Zhai Wei, Sun Xiaoming, He Xiaoping, Su Liwei, Wu Youliang and Dong, Y.X., 2007. Geochemistry of ore forming fluid and metallogenic mechanism of Axi low-sulfidation gold deposit in Xinjiang, China. *Acta Geologica Sinica*, 81(5): 659–670 (in Chinese with English abstract).

Zhang, Z.W., Wu, C.Q., Yang, X.Y., Zheng, C.F., and Yao, J.H., 2015. The trinity pattern of Au deposits with porphyry, quartz–sulfide vein and structurally-controlled alteration rocks in Ciemas, West Java, Indonesia. *Ore Geology Reviews*, 64: 152–171.

Zheng Chaofei, Zhang Zhengwei, Wu Chengquan and Yao Juanhua, 2014. Sulfur Isotope Composition of Ciemas Gold Deposit in West Java, Indonesia. *Acta Geologica Sinica* (English Edition), 88(s2): 852–853.

About the first author

ZHENG Chaofei, male, born in 1988 in Xingtai City, Hebei Province; Doctoral student of Geochemistry, Chinese Academy of Sciences; He is now interested in the study on the geology and geochemistry of gold deposits and zinc-lead deposit. Email: zhengchfei@gmail.com.